

Deep Predictive Motion Tracking in Magnetic Resonance Imaging: Application to Fetal Imaging

Ayush Singh¹, Seyed Sadegh Mohseni Salehi¹, and Ali Gholipour¹, *Senior Member, IEEE*

¹Department of Radiology, Boston Children's Hospital; and Harvard Medical School, Boston MA 02115

Fetal magnetic resonance imaging (MRI) is challenged by uncontrollable, large, and irregular fetal movements. Fetal MRI is performed in a fully interactive manner in which an experienced MRI technologist monitors fetal motion to prescribe slices in right angles with respect to the anatomy of interest. Current practice involves repeated acquisitions to ensure diagnostic-quality images are acquired; and the scans are retrospectively registered slice-by-slice to reconstruct 3D images. Nonetheless, manual monitoring of 3D fetal motion based on displayed 2D slices and navigation at the level of stacks-of-slices (instead of slices) is sub-optimal and inefficient. The current process is highly operator-dependent, requires extensive training, and yet significantly increases the length of fetal MRI scans which makes them difficult for pregnant women, and costly. An automatic real-time image-based motion monitoring system can significantly improve fetal MRI. With that motivation, we have developed a new *real-time image-based motion tracking* technique in MRI using deep learning, which is presented in this paper. Through a combination of spatial and temporal encoder-decoder networks, our system learns to predict 3D pose of the fetal head based on dynamics of motion inferred directly from sequences of acquired slices. Compared to recent works that exploited deep *convolutional neural networks* to estimate *static* 3D pose of the subject from slices, our method is a *recurrent neural network* that learns to predict *dynamics* of 3D motion. Our temporal encoding-decoding is based on sequence to sequence learning using long short term memory modules. We compared our trained network on held-out test sets (including data with different characteristics, e.g. different age ranges, and motion trajectories recorded from volunteer subjects) with networks designed for estimation as well as methods adopted to make predictions. The results of all estimation and prediction tasks show that we achieved reliable real-time fetal head motion tracking in fetal MRI. This technique can be augmented with deep learning based fast anatomy detection, segmentation, and image registration techniques to build real-time fetal MRI motion tracking and navigation systems.

Index Terms—Motion tracking, Image registration, Pose estimation, Deep learning, CNN, LSTM, Seq2Seq, MRI, fetal MRI.

I. INTRODUCTION

A. Motivation

MAGNETIC Resonance Imaging (MRI) is a relatively slow imaging technique that is, therefore, extremely susceptible to subject motion. To deal with this limitation,

when MRI scans are performed, subjects are instructed to stay completely still. To scan newborns and young children, this requires strategies such as feed-and-wrap, padding, or training, whichever is applicable, to restrain or reduce motion [1], [2], [3]. There has been extensive research and development in motion-robust sequences and motion correction techniques in MRI (e.g. [4], [5], [6], [7], [8], [9], [10]), but the techniques are rather limited in their application based on the patient population, the type and extent of motion, and the type of MRI sequences. For example none of the current techniques can be directly used for motion monitoring in fetal MRI.

Among all rapidly-emerging MRI applications, fetal MRI is, arguably, one of the most challenging, due to uncontrollable, large, and irregular fetal movements [11]. In particular in mid gestation fetuses have relatively large space to stretch and rotate in large angles. Fetal motion is complex and cannot be monitored or tracked by external sensors or camera systems or accounted for by cardiac and/or respiratory gating. Fetal MRI motion correction techniques have thus relied upon retrospective image registration solely based on image information [12], [13], [14], [15], [16], [17], [18], [19], [20].

Slice-to-volume registration, which has been widely used in retrospective fetal MRI reconstruction, is inherently an ill-posed problem [21]. It has a limited capture range as it relies on iterative optimization of intensity-based similarity metrics that are only surrogate measures of alignment between a reference volume and slices. Moreover, a motion-free reference volume may or may not be readily available. To increase capture range, one may use grid search on rotation parameters along with multi-scale registration [22]; but this approach is also computationally expensive as it is based on iterative numerical optimization at test time. For reference volumes, one may use age-matched atlases, e.g. [23], and perform atlas-based registration, e.g. [22], [24], however these methods are also computationally expensive for real-time application.

To improve capture range and the speed of subject-to-atlas image registration, in a recent work [25], deep regression convolutional neural networks (CNNs) were trained to estimate 3D pose of the fetal brain based on image slices and volumes. Partly inspired by [25], in this paper we present a novel *deep predictive motion tracking* framework based on long short term memory (LSTM) [26] recurrent neural networks (RNNs). While the technique in [25] addressed *static* 3D pose estimation only (based on regression CNNs), our work here addresses *dynamic* 3D motion tracking in MRI, for the first time, using RNNs, exploiting LSTM modules and innovative learning strategies, that are explained in this paper.

Manuscript received September 22, 2019. This study was supported in part by the National Institutes of Health (NIH) grants R01 EB018988 and R01 NS106030, and by a Technological Innovations in Neuroscience Award from the McKnight Foundation. The content is solely the responsibility of the authors and does not necessarily represent the official views of the NIH or the McKnight Foundation. Corresponding author: Ayush Singh (email: ayush.singh@childrens.harvard.edu). Relevant code can be found at: github.com/singhay/DeepPredictiveMotionTracking

Our proposed method learns to predict motion trajectory based on MRI time series. While motivated by an unmet need in the application domain, our technique was inspired by the most recent advances in computer vision, which are reviewed next, where we also review the related work in fetal MRI and MRI motion tracking, and discuss our contributions in detail.

B. Related Work

Pose estimation using 2D (digital) images and videos has been extensively researched in computer vision, where algorithms aim to find 3D pose of objects with respect to camera. Work in this area can be studied in two main groups: methods that predict key points leveraging object models to find object orientation, e.g. [27]; and methods that predict object pose directly from images to discrete pose space-bins, e.g. [28], [29] and [30]. While the majority of pose estimation techniques have been designed as classification methods, the problem has been recently modeled and solved by regression deep neural networks [31]. Deep CNNs have shown great performance in pose estimation in recent years, e.g. [31], [32], [33], [34].

Three-dimensional pose estimation from 3D or stack-of-2D medical images has also been recently addressed using CNNs. For a review of the related pose estimation and registration methods we refer to [25]. For fetal MRI, in particular, deep regression CNNs were designed for slice-to-volume registration on non-Euclidean manifolds [35], and used to estimate transformation parameters for fetal head position to reconstruct fetal brain MRI volumes from slices [36]. Real-time fetal head pose estimation was achieved in [25] by multi-stage loss minimization using mean squared error and geodesic loss, and used for image-to-template and inter-subject rigid registration.

The above-referenced techniques treat image slices independently. Therefore, while they are powerful in that they learn to predict head position based on single slices, they ignore the rich information content of stack of sequentially acquired slices and the dynamics of head motion. Consequently, these methods require good initialization or regularization to estimate 3D views from slices. While pose estimation methods can be combined with iterative slice-to-volume registration for head motion tracking, e.g. [19]; a natural, promising extension of this line of work is dynamic image time series modeling, which has been the subject of our work presented in this paper.

Traditional time series prediction models such as ARIMA (auto-regressive integrated moving average; seasoned, and non-seasoned) expect data to be locally stationary. These are regression models that make strong assumptions about data to predict future values based on past observations. These models shall be paired with other techniques to effectively process and use image time series information; but this integration may not be straightforward. RNNs [37], on the other hand, can handle non-stationary and nonlinear data. They offer end-to-end frameworks to take images as input and make predictions, and are flexible in terms of the corresponding objectives.

Variants of RNNs such as networks based on LSTM [26] have the capacity to learn the amount of information to remember and forget from past sequences. This makes them less susceptible to unaccounted cases that cannot be easily

handled by graph designer of dynamic Bayesian networks (DBNs) [38]. Compared to traditional models where error propagation leads to error accumulation in long-term prediction, advanced LSTM-based methods, such as sequence-to-sequence (Seq2Seq) learning [39], can reliably predict variable time steps with long prediction horizons.

Deep predictive motion tracking using RNNs based on video sequences has also been widely studied in robotics and computer vision, e.g. [39], [40], [41]. A review of these studies is beyond the scope of this paper, but we briefly review some representative methods and studies. The first group of techniques based on siamese networks detect and use regions close to object locations to track objects, e.g. [42], [43]. Large datasets can be used to train these networks for feature extraction and region proposals for simultaneous one-shot detection (classification) and online tracking (regression) [44]. Early performance gains in accuracy were obtained by passing features from an object detector to LSTMs [45]. In the LSTM category, the Real-time Recurrent Regression (Re³) network [46] combined non-differentiable cropping and warping with feature extraction using a residual network (ResNet), and passed them to LSTM for object tracking.

C. Contributions

In this paper we present, for the first time, a dynamic motion tracking framework for MRI based on deep learning. Compared to recent developments in static 3D pose estimation from MRI slices and volumes based on CNNs [25], [36], in this work we exploit RNNs for predictive dynamic motion tracking. Compared to motion tracking in computer vision, robotics, digital image and video processing, where 3D pose or projected motion of objects is modeled and estimated based on 2D+time images (videos) with respect to cameras, in this work we deal with 3D rigid motion of anatomy (in the scanner/world coordinate system) from stacks of sequentially acquired slices (3D+time image time series). Consequently, while the majority of human pose tracking or video object tracking methods are formulated and solved as classification problems in a parameter space, we solve a regression problem where 3D rigid motion parameters are estimated based on features directly extracted from MRI time series.

Our contributions are threefold: 1) we developed a learning-based, image-based, real-time dynamic motion tracking in MRI based on deep RNNs: Our model encodes motion using LSTM after extracting spatial features from sequences of input images using CNNs, estimates objectives for given images and creates a context vector that is used by LSTM decoders to regress against angle-axis representation and translation offset to predict 3D rigid body motion. The network constitutes multiple representation heads [47] to avoid over-fitting to either rotation or translation parameters. 2) we devised multi-step prediction by feeding output of previous decoder as input to current decoder combined with the context vector. 3) we trained and tested networks on sequences with masked slices that are slices lost due to intermittent fast intra-slice motion.

We developed and tested our method for fetal head motion tracking in fetal MRI, which is a very challenging problem due

to the wide range of fetal head positions and motion; but the technique can be used in broader applications. The fetal brain MRI data intrinsically shows a wide feature range due to inter-subject variability and different age of fetuses at the time of MRI scans as well as rapid changes that occur to the fetal brain during gestation. To train and test models we used held out scans of 36 and 40 fetuses correspondingly, randomly chosen from the sample population (scanned at different gestational ages). We simulated motion and also used motion trajectories from sensor recordings of head motion of volunteer subjects to test the generalization capacity of our trained network. We set up a probing task to examine temporal and spatial dependency of our trained model. Our experiments showed that the trained model not only estimated motion parameters but also was able to make long term predictions based on sequence of fetal brain images with both simulated and real motion in the test set. The paper is organized as follows: the details of our network and methods are discussed next. Then, the experiments and experimental results are described in Section III; which are followed by a discussion and conclusion in Section IV.

II. METHODS

A. Problem formulation

Our goal is to take in a sequence of slices X_1, X_2, \dots, X_n ($X_n : N \times N$) sampled sequentially (in time) from 3D fetal anatomy (usually acquired in an interleaved manner) in an MRI scan to estimate and predict 3D pose (rotation and slice position) Y_1, Y_2, \dots, Y_{n+m} of the fetal brain for current n timesteps as well as future m timesteps. Our technique does not put any restriction on the values of n and m . Although n is limited by the number of input slices, m can be variable *i.e.* either less, equal or greater than n . Note that these slices are not rotation of initially sampled slices in a particular sequence, rather they represent slices from a stack of sliced anatomy while the anatomy moves in 3D in between slice acquisitions. For the purpose of this study we assume that the fetal brain is extracted (segmented) in each slice using a real-time fetal brain MRI segmentation method [48]. For the development and evaluation of predictive motion tracking, we also assume that center-aligned slices are extracted from 3D fetal brain images reconstructed and segmented using the existing techniques [15], [49].

Figure 1 shows how the data is pre-processed and prepared for fetal head motion tracking. The region-of-interest (RoI), which is the fetal brain in this study, is first extracted using a real-time brain extraction method [48] and the slices are cropped, masked, and center-aligned to form a 3D stack. Slices that are corrupted by intra-slice motion appear black as the brain extraction method does not generate a mask for those slices. Fetal motion thus appears as inter-slice motion with occasional black (masked) slices due to intra-slice motion. The problem is, hence, to find 3D rigid transformations, T_i s, of the fetal head at the times corresponding to slice (X_i) acquisitions.

A 3D rigid-body transformation T has 6 degrees-of-freedom represented by a vector \mathbf{t} comprising of three translation (t_x, t_y, t_z) and three rotation ($\theta_x, \theta_y, \theta_z$) parameters. For 3D rotation representation we follow [25] which uses Euler's

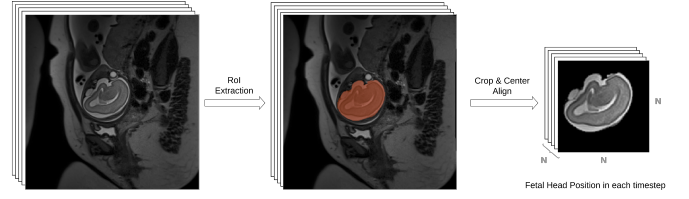


Figure 1: The Region-of-Interest (RoI), here the fetal brain, is extracted using a real-time segmentation technique, e.g. [48], cropped, center aligned, and intensity normalized to form a volume of stacked slices for deep predictive fetal head motion tracking.

theorem and the Rodrigues rotation formula to represent the 3×3 rotation matrix by the angle-axis representation where the rotation axis is its unit vector and the angle in radians defines its magnitude. Since we center align the images in the pre-processing step, the translation parameters are assumed to be known a priori, which allows us to constrain our parameter space to the slice position z and three rotations ($\theta_x, \theta_y, \theta_z$) represented by the angle-axis formalism. The method in [25] can be used to estimate a priori translation parameters.

B. Deep regression RNN for predictive motion tracking

As shown in Figure 2, our deep RNN model for predictive slice-level motion tracking in MRI is built of two main parts: an encoder and a decoder. The encoder network, which is composed of deep CNN blocks followed by unidirectional LSTM and P blocks, takes a sequence of slices X_1, \dots, X_n as input, and estimates a sequence of n transformations as well as an encoder state, which is fed into the decoder network. Conditioned on the encoder state, the decoder network, which also constitutes LSTM and P blocks, predicts transformations for future time steps m . A P block involves three representation heads, each consisting of a dense block and an activation function for regression at the output layer. The activation functions are $\pi \tanh$ for the rotation parameters θ and rectified linear unit (ReLU) for slice position shown here by z . In the sections that follow we discuss each of the network components and the details of training.

C. Encoder: Spatial

For spatial encoding, convolutions are applied to each slice X_n of a sequence where n is the index of the slice in the sequence. Figure 3 shows the architecture of the spatial encoder network and describes its details. Through weight sharing the same CNN is trained and applied to all slices. This means there is no dedicated network for each timestep. Instead, during training, shared kernel weights of the CNNs are updated to account for variations in all timesteps. The spatial-invariance trick, achieved by weight sharing, allows the spatial encoder CNN to learn and encode slice features, and pass those into the temporal encoder to make predictions.

D. Encoder: Temporal

Just as CNNs share weights across space, RNNs share weights across time allowing them to learn patterns from

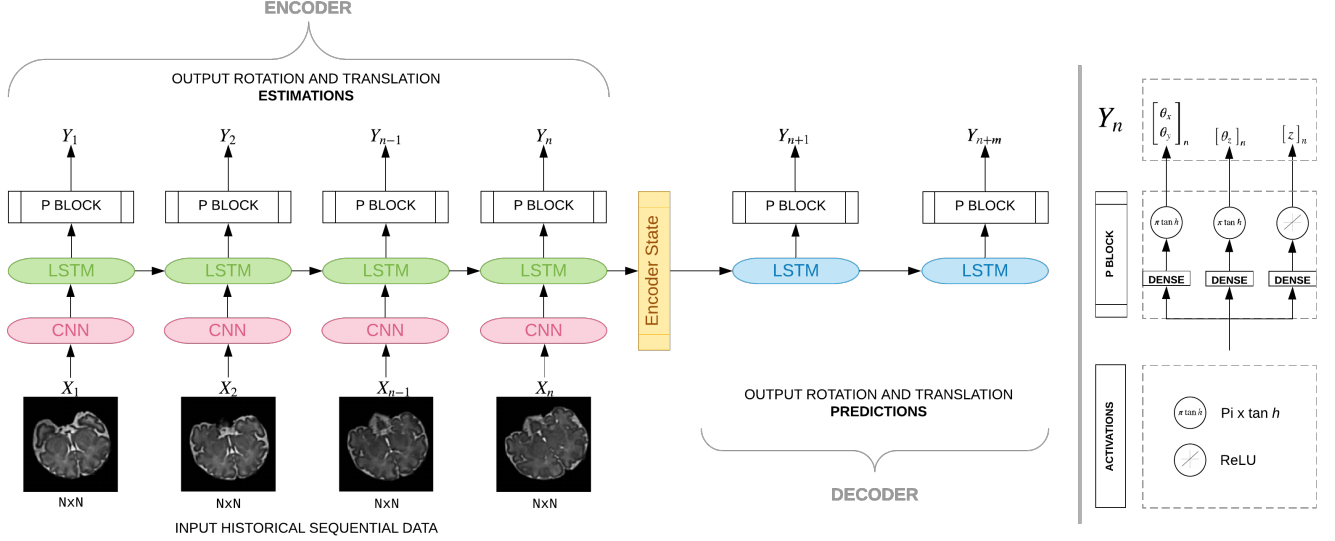


Figure 2: Our many-to-many Seq2Seq model that takes as input sequence of slices and estimates angles as well as predictions. Multiple LSTM units are shown since we unroll our network. All units of the same type and color share weights, hence they get the same gradient update during training. This model comprises of an encoder and a decoder component. The encoder, which contains spatial encoder (CNN) blocks followed by a temporal encoder that contains LSTM units and P blocks, encodes and learns sequence-of-image features to estimate position parameters. The encoder state is fed into the decoder network which comprises of LSTM units followed by P blocks. Each P block has three heads with $\pi \tanh$ activation for the rotation parameters and ReLU activation for the slice position.

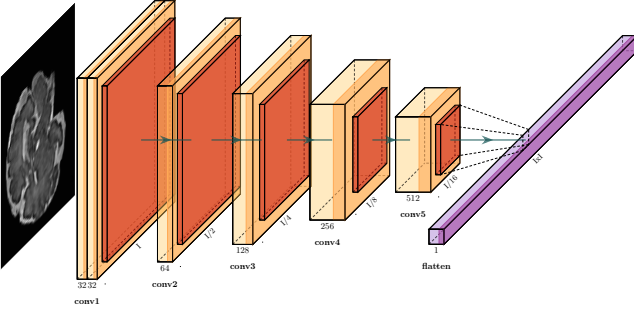


Figure 3: The architecture of the spatial encoder CNN blocks of our deep predictive motion tracking model shown in Figure 2. Each encoder performs 3×3 convolutions followed by batch normalization, PReLU (instead of ReLU to avoid dead ReLU phenomena) and MaxPooling that down-samples the image in half, extracting local dependencies and reducing computation in downstream layers. This enables fine-grained feature preservation. The number of filters is doubled in each layer until it reaches 512. Finally, each CNN flattens the feature map and transfers it as spatial encoding of a particular time step n in the sequence to the LSTM layer of the encoder.

sequential data. Since vanilla RNNs face vanishing gradient problem that makes it difficult to propagate gradients back in time, we used LSTM [26], which also learns what to remember and what to forget. This is important to learn the anatomy and how it is sampled by slices over time using the gating mechanism. Based on encoded image features from the CNNs, the LSTM layer learns to estimate the state of the anatomy, i.e. the 3D pose of the anatomy and its sampling.

LSTM has three primary components: W, U, b ; where W is

the recurrent connection between previous and current hidden layers, U connects inputs to current hidden layer and b is bias:

$$LSTM_{encoder} : X_n, h_{n-1}, c_{n-1} \longrightarrow h_n, c_n \quad (1)$$

$$i_n = \sigma(W_i X_n + U_i h_{n-1} + b_i) \quad (2)$$

$$f_n = \sigma(W_f X_n + U_f h_{n-1} + b_f) \quad (3)$$

$$o_n = \sigma(W_o X_n + U_o h_{n-1} + b_o) \quad (4)$$

$$\hat{c}_n = \tanh(W_h X_n + U_h h_{n-1} + b_{\hat{c}}) \quad (5)$$

$$c_n = f_n \odot c_{n-1} + i_n \odot \hat{c}_n \quad (6)$$

$$h_n = o_n \odot \tanh(c_n) \quad (7)$$

For each time step n , the memory cell $c_n \in \mathbb{R}^n$ is called as it controls exposure of the previous memory c_{n-1} with current input X_n . This is done by combining c_{n-1} multiplied by the forget gate f_n , with the computed hidden state h_n multiplied by the input gate i_n . These are called gates because they squash values between 0 and 1 using the sigmoid activation function σ . The element-wise multiplication \odot controls how much of information is let through: The input gate controls how much of the current input goes through; the forget gate controls the throughput of the previous state; and the output gate controls the amount of exposure of the internal states

to the next timesteps (or the downstream layers). All gates have dimensions equal to that of the hidden layer h_n , which is computed by multiplying the hyperbolic tangent \tanh of memory c_n with the output o_n . \hat{c}_n is the candidate hidden state that connects the current input X_n to the previous hidden state. One can ignore old memory completely (all zeros f_n) or ignore states (all zeros in i_n), but we chose to store nuances of changes in data over time thus the values were between 0 and 1.

Flattened feature maps pass from the spatial encoder to the unidirectional LSTM network. Output of each time step of the encoder and decoder LSTM go through dense fully-connected layers to get estimated and predicted parameters. The last non-linear function with weights $W_{\theta_{xyz}}$ on top of the dense layer is $\pi \tanh$ which limits the output of each element from $-\pi$ to $+\pi$ and simulates the constraints of each element of the rotation vector (θ_x, θ_y) and θ_z independently:

$$\theta_n^{xyz} = \pi \tanh(W_{\theta_{xyz}} o_n + b_{\theta_{xyz}}) \quad (8)$$

The slice index (z) estimator head with weights W_z contains a scalar, as the network tries to estimate the continuous slice index along with its orientation. For inference, the continuous index is rounded (i.e. $\lfloor z \rfloor$) to infer a discrete slice number.

$$z_n = \max(0, W_z o_n + b_z) \quad (ReLU) \quad (9)$$

E. Decoder: Modeling variable and long term predictions

The conventional approach to predict sequential data is to use n steps of the sequence from the past to predict the immediate future time step $n + 1$ and repeat recursively to make future predictions up until the desired prediction horizon. This model, however, shows limited multi-step prediction performance in applications such as image-based motion tracking as it faces issues raised by compounding errors especially when initial predictions may exhibit relatively large amounts of error. To mitigate this issue and make variable-length, long-term predictions we follow the idea of sequence to sequence learning [39]. In this approach, an LSTM encodes the input sequence of images into a fixed dimension vector, and another LSTM decodes the target sequence from this vector. The advantage of this technique is that we no longer need to rely on encoder estimates to predict variable-length time steps of the future as encoder and decoder are two separate LSTM networks. Figure 2 shows our LSTM network unrolled.

Each decoder is trained to predict parameters of the following step. Therefore, input to the first decoder is the estimation vector \hat{Y}_n of the last slice X_n from the encoder and the rest of the decoder takes output of the previous decoding step \hat{Y}_{m-1} so that over time the model learns to correct its own mistakes.

$$LSTM_{decoder} : \hat{Y}_{n+m-1}, h_{n+m-1}, c_{n+m-1} \longrightarrow h_{n+m}, c_{n+m} \quad (10)$$

The goal of decoding is to model the conditional probability of $P(Y_1, \dots, Y_{n+m} | X_1, \dots, X_n)$. The decoder uses h_n, c_n from encoder as its initial state to compute $P(Y_{n+m})$. However the decoder does not directly model $P(Y|X)$, its power comes from modeling probability of current output with respect to

all previous timesteps $P(Y_{n+m} | Y_{<n+m}, X_n)$ where $Y_{<n+m}$ represents output from 1 to $n + m - 1$. The posterior probability of the output state given inputs, with model parameters γ , is as follows

$$P_\gamma(Y|X) = \prod_{n=1}^{n+m} P_\gamma(Y_n | Y_{<n}, X) \quad (11)$$

F. Splitting into multiple heads

The coupling between in-plane and out-of-plane rotation with the slice select direction and slice location z hinders optimization and learning [35]. To alleviate this issue, we divided the rotation θ regression heads from Equation (8) and added a hidden layer one each for θ_{xy} and θ_z as follows:

$$\theta_n^{xy} = \pi \tanh(W_{\theta_{xy}} \tanh(W_{\theta_{xyz}} o_n + b_{\theta_{xyz}}) + b_{\theta_{xy}}) \quad (12)$$

$$\theta_n^z = \pi \tanh(W_{\theta_z} \tanh(W_{\theta_{xyz}} o_n + b_{\theta_{xyz}}) + b_{\theta_z}) \quad (13)$$

which changes minimizing our loss calculation from

$$L_{Total} = L_{\theta_{xyz}} + L_z \quad (14)$$

to

$$L_{Total} = L_{\theta_{xy}} + L_{\theta_z} + L_z \quad (15)$$

For training, we minimized loss for both estimation and prediction $L_{Total} = L_{estimation} + L_{prediction}$ where $L = \|Y - \hat{Y}\|_2$. We used \tanh as activation of this hidden layer as its derivative provided stronger gradients for regression tasks compared to $ReLU$ or $sigmoid$ functions. Our experiments showed that this helped with learning to predict θ_z more effectively.

III. EXPERIMENTS

To train, test, and evaluate our method we conducted experiments with real fetal MRI data with simulated motion and motion tracking data of volunteers who moved inside scanner while motion parameters were recorded using an external motion tracking sensor. We divided our experiments into estimation for 10 timesteps and prediction for 10 timesteps. We evaluated our trained model for generalization, robustness, and latency; and compared our results against pose estimation networks in particular those based on SVRNet [35], PoseNet [25], and our baseline models for estimation and prediction. In this section, we describe the fetal MRI data and its pre-processing first; and then the details of our experiments that involved generating the training data and the results of estimation and prediction for both simulated and real motion trajectories.

A. Fetal MRI dataset

The fetal MRI dataset consisted of 76 reconstructed T2-weighted fetal MRI scans of fetuses scanned at a gestational age (GA) between 21 and 37 weeks (mean=30.1, stdev=4.6) on 3-Tesla Siemens Skyra scanners with 18-channel body matrix and spine coils. Repeated multi-planar T2-weighted single shot fast spin echo scans were acquired of the moving fetuses. Brain masks were automatically extracted based on the real-time algorithm in [48]. The scans were automatically cropped

around the fetal head RoI (based on the masks) and were then processed using slice-by-slice motion correction to reconstruct a super-resolved 3D volume [15], [17]. Final 3D brain masks were then generated on the reconstructed images using Auto-Net [49] and manually corrected in ITK-SNAP [50] as needed.

Brain-extracted reconstructed volumes were then registered to a spatiotemporal fetal brain MRI atlas described in [23]. We normalized the intensity of the reconstructed images to zero-mean, unit-variance. The set of 76 scans was randomly split into 30, 6, and 40 for training, validation, and test, respectively; where the GA range spanned over 29 to 35 weeks for the training set, and from 26 to 37 weeks for the test set. We intentionally chose a narrower age range for the training set than the test set to examine the generalization capability of the trained models. To generalize well, the trained models had to account for both intrinsic inter-subject anatomical variations (due to different fetuses in the training and test sets) and anatomical variations due to different maturation levels of fetuses scanned at different GA ranges.

B. Generating the Training Data

To achieve our goal of predicting motion and slice position from sequences of slices, we aimed to train networks to learn the patterns of slice sampling and fetal head motion in reference to the fetal brain anatomy while it develops during gestation. To generate the training, validation, and test data for this purpose, from the pre-processed fetal MRI data, we generated sequences of fetal MRI slices with motion. This involved two sampling components: spatial sampling of slices and temporal sampling of spatial slices to model fetal motion. For slice excitation and spatial sampling, we sampled sequentially along permuted Z axes with 5 mm slice gap to account for fetal MRI acquisitions that are interleaved.

For temporal sampling to generate dynamic transformations corresponding to fetal motion, we exploited curve fitting with smoothing cubic Splines for each of the rotation angles. In this scheme, smoothing cubic splines generated different motion trajectories by interpolating curves between randomly-generated control points. The number of control points varied to control speed of motion. This was analogous to how fast or slow the fetus moved between scans. Further, to account for fast motion that disrupts slice encoding, we randomly masked a timestep in all slices. This resembled intra-slice motion as the brain masking technique in [48] generated all-zero masks for motion-corrupted slices. Figure 4 shows five 10-timestep sequences generated from the reference (GT) image sequence with random patterns and different speeds of motion.

We sampled 32 sequences for each subject in the training set 300 times (epochs). This led to 30 subjects \times 32 sequences (1 batch size of 5 speed categories) \times 300 times = 288,000 sequences for training, where speed of motion was controlled by the number of smoothing spline control points sampled from a normal distribution ($\mu = 6.4$, $\sigma = 1.36$, bounds=[4, 8]). The initial rotation matrices were bound to the $[-60, 60]^\circ$ range, and the rotation parameters $\theta_x, \theta_y, \theta_z$ were sampled from a zero-mean normal distribution in the $[-30, 30]^\circ$ range. This led to maximum rotation bounds of $[-90, 90]^\circ$. For validation and

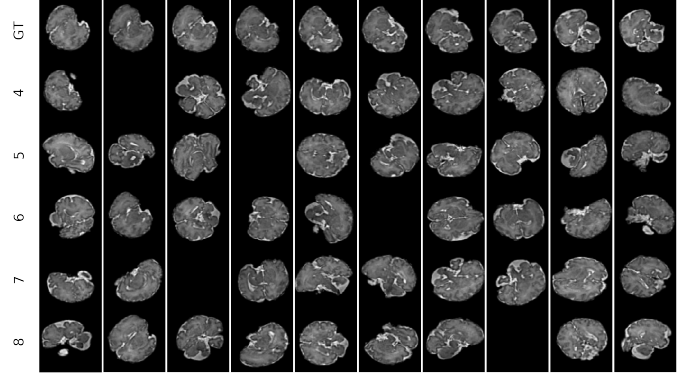


Figure 4: A demo of five sequences of 10 timesteps each generated with different speeds of motion (corresponding to the number of control points from 4 to 8) from the original 3D reconstructed fetal brain MRI scan of GA 35 weeks (shown at the top row). Randomly masked slices indicate slices corrupted by intra-slice motion.

hyper-parameter tuning we used 6 subjects not in the training set. Following the same sampling strategy used in the training set, this led to $6 \times 32 \times 300 = 57,600$ sequences for validation.

C. Test Datasets

To test and compare algorithms, we sampled 32 sequences per speed of [4, 8] where we followed the spatial and temporal sampling strategies described in the previous section. This resulted in a total of 40 test subjects \times 32 samples = 1280 sequences of 10 timesteps each for test. Even though our main goal was to evaluate one-step ahead prediction, having 10 timesteps allowed us to test efficacy of the model on long-term predictions. While our training data was limited to sequences generated from fetal MRI scans using the described procedure, to evaluate the generalization capacity of the trained models for new (unseen) patterns of motion, in addition to the test set described above, we used motion data recorded using head motion tracking sensors [51] from 10 volunteers. Rigid 3D transformation parameters were recorded in the scanner as volunteers moved their head with different patterns and speeds during scans. We applied these motion trajectory parameters to each of the 40 fetal test subjects, which led to a total of 400 new sequences with motion patterns that differed in character from the motion patterns of the training data.

D. Implementation and Experimental Details

We implemented our model in Keras based on Tensorflow and trained and tested on an NVIDIA GeForce 1080 Ti. We used the mean square error loss and the RMSprop optimizer with initial learning rate of 0.001 ending in 0.00001 over the course of 300 epochs decreasing learning rate when loss plateaued for 50 consecutive epochs. Due to the temporal nature of MRI slice acquisitions and the fact that the boundary slices did not include sufficient anatomical features, we limited estimation and prediction of motion trajectories (in training and test) to slices $s_i; i \in [0.4S, 0.9S]$, where S was the total number of slices in each reconstructed volume. Latency for prediction on our hardware was $\sim 1.42ms$ per data point

where each sequence comprised of 10 slices and outputs were 10 estimations and 10 predictions. Considering the slice acquisition time of ~ 1.5 seconds for T2-weighted MRI and $\sim 80ms$ for echo-planar imaging, this is real-time.

We conducted experiments and evaluated our model in both estimation and prediction tasks. For estimation, we compared our model (with 4.7M parameters) with two state-of-the-art fetal MRI pose estimation methods, *i.e.* an 18-layer residual network (ResNet) with two regression heads, one for angles θ and the other for slice location z , based on PoseNet [25] (with 11M parameters), and a VGG16-style network based on SVRNet [36] (with 14.7M parameters). Since SVRNet chose VGG16 among several other models, namely GoogleLeNet, CaffeNet, Inception v4, NIN, and ResNet, we only compared against VGG16 as according to [36] it generated the lowest MSE among those alternatives.

For prediction, we conducted experiments for one-step and multi-step ahead predictions. To implicitly model motion states (*i.e.* to sense and incorporate motion velocity and acceleration) we needed a window size of at least three timesteps. In our experiments we used a window size of 10 for estimation and prediction. For multi-step prediction, we limited our evaluation to 10 timesteps in the future although this was a choice and not a theoretical limit on the prediction horizon. We compared our predictor against three baselines: 1) a naive predictor that used estimation at current time as one-step ahead prediction (referred to as zero velocity predictor); 2) an auto-regressive model that recursively used its own predictions in a sliding window of size 10 to predict multi-step motion trajectories; and 3) a predictive model that we adopted based on the network proposed in [52]. In this model (with 44M parameters), the data was passed directly into an LSTM without spatial feature encoding, thus we refer to it as directLSTM.

E. Results

Figure 5 shows 10 estimated and 10 predicted timesteps for a train case and a test case compared to the ground truth slices in the top rows. The predicted rotation was accurate after multiple timesteps. Table I shows average loss of estimation and prediction tasks for ablation studies and the comparisons to baseline and alternative methods. We compared our “full model” trained with sequences with masked slices (resembling slices corrupted by intra-slice motion) and split loss explained in Section II-F against our “baseline” which was trained without masked slices in the training set sequences and without split heads, and “masked bl” which was trained with masked slices but without the split loss functions. The best results in each comparison, shown in bold, show that our full model outperformed the baselines and all other models in both estimation and prediction tasks. The low standard errors of our model show its consistent and robust performance.

Figure 6 shows the squared error of multi-step prediction per timestep (estimation for time 10 and predictions for times 11 to 19), where timepoints 1 to 10 were the input to the model. For estimation the auto-regression model showed an error comparable to our model, but as the prediction horizon increased, our model showed lower error than all baselines.

Model	μ error	σ_μ	σ_μ time	σ_μ age	σ_μ speed
VGG16	129.33	11.74	3.72	3.48	9.51
Resnet18	82.60	5.76	3.55	1.31	3.34
Our baseline	20.19	2.57	1.21	2.23	2.06
Our masked bl.	9.10	2.31	1.11	1.92	2.45
Our full model	3.55	0.22	0.17	0.05	0.23
directLSTM	103.20	3.09	0.97	13.52	5.80
Zero velocity	74.14	1.09	0.86	1.77	1.32
Auto regressive	96.77	1.66	0.69	1.83	2.17
Our baseline	33.51	2.35	1.17	1.23	1.11
Our masked bl.	11.28	1.28	1.17	0.23	0.51
Our full model	8.07	0.72	0.42	0.39	0.59

Table I: Mean squared error (μ error) for estimation and prediction along with the overall standard error of mean (σ_μ) and the standard error of different timesteps, ages, and speed of motion for the test data. The top part of the table compares estimation models and the bottom part compares prediction models. In these comparisons we also tested our model trained without any masked slices in the sequences, referred to as the “baseline”, our second baseline trained with sequences with masked slices but without the split heads and loss function explained in Section II-F (referred to as “masked bl.” model) and our “full model” trained with both masked slices and the split loss function. Significant reduction in both estimation and prediction errors were achieved by our full trained model compared to baselines and all other compared models. Low standard errors show that our model performed consistently, and was robust to variations in data, timesteps, gestation age, and speed of motion.

In the next sets of experiments, we evaluated our model for 1) its generalization performance for our test data that included subjects scanned at gestational ages not included in the training set; 2) its performance for different speeds of motion; 3) its robustness in the presence of intra-slice motion (*i.e.* lost slices in the input sequence due to fast motion that disrupted signal during slice encoding); and 4) its generalization and robustness to motion patterns that were different from the motion patterns in the training data (*i.e.* motion patterns recorded from volunteer subject experiments).

Figure 7 shows boxplots of squared error of estimation and prediction tasks for 10 timesteps grouped by gestational age and datasets. The consistency in error statistics across test and train datasets and GA, indicate that the trained model was robust and generalized well to the test data.

Table II shows mean squared errors of estimation, one-step and multi-step prediction for test data grouped by the location of a lost slice (due to intra-slice motion) in the input slice sequence. This table compares the performance of two models: our model trained without any missed (masked) slices in the training sequences (referred here as the baseline); and our full model trained with randomly missed (masked) slices in the training set. These results show that 1) in the baseline model, both estimation and prediction errors were higher when the lost slice was closer to the end of the input sequence; *i.e.* missing slice 10 in the sequence led to much higher errors (shown in red) compared to missing slices in earlier locations; and 2) Our full model performed better than the baseline with much more consistent and robust performance. These show that when our model was trained with randomly masked slices in the training sequences, it learned to rely less on the last slices in the sequence to gain robustness in the presence of intra-slice motion.

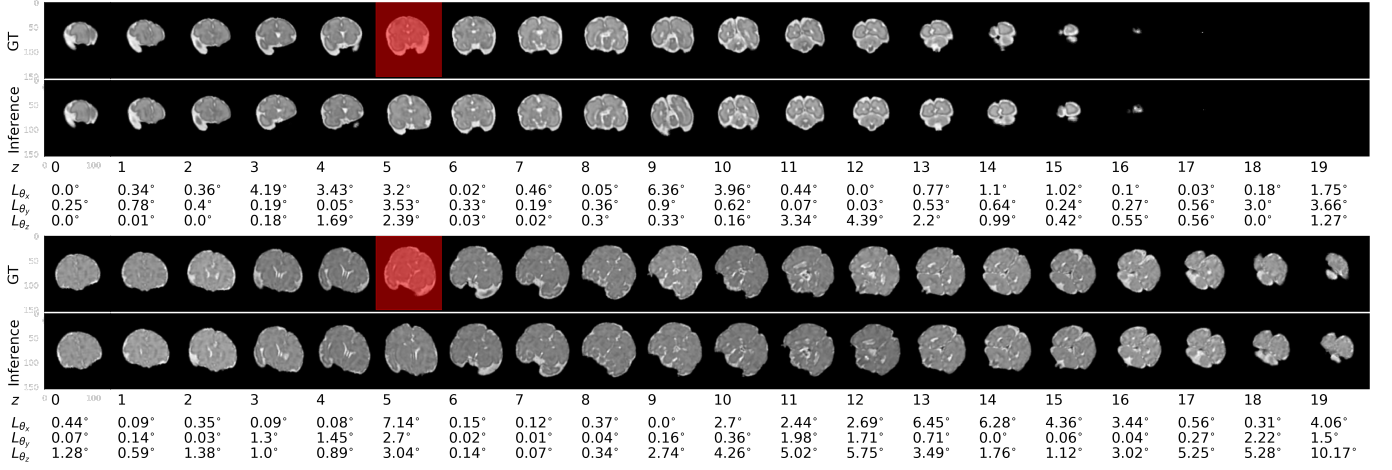


Figure 5: Inference (i.e. estimation for the first 10 timesteps and prediction for the rest of the 10 timesteps) in the bottom rows has been compared to the ground truth sequence in the top rows for scans of two fetuses: the first figure is a scan of a 28-week, and the second figure is a scan of a 36-week GA fetus from the test set. Errors have been shown underneath each timestep. In these figures the slices shown with red masks were masked in the input sequence. It can be seen that the estimated slices (in the bottom rows) corresponding to the masked slices, showed relatively larger error, but the masked slices did not have a major effect on predictions. Slight increase in prediction error with prediction time horizon was seen in the test sequence, but the predictions were overall accurate.

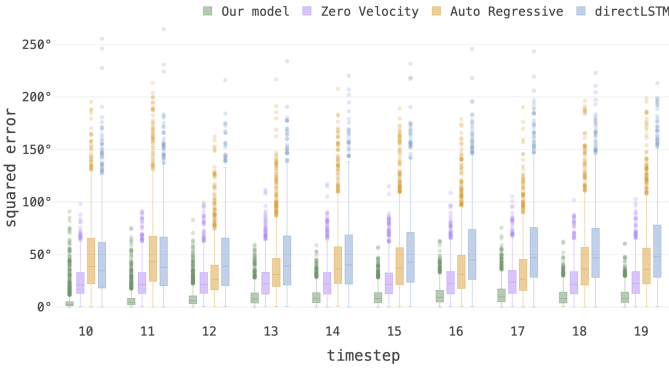


Figure 6: Boxplots showing the statistics of the squared rotational error computed as: $(\theta_{xyz} - \hat{\theta}_{xyz})^2$ for prediction per timestep. Our model outperformed all the prediction baselines (zero velocity, auto-regressive, and directLSTM). While the auto regressive model showed comparable error to our model at the first timestep, its average error increased at other timesteps due to compounding errors.

Our final experiment focused on the generalization capacity of the trained model for motion trajectories recorded from volunteer subjects that were never used in training. Figure 8 shows the squared prediction error for different timesteps for the test data with the real, recorded motion trajectories, obtained from our full model and other predictor models. The results show that our model generated very low multi-step prediction errors, whereas all other methods showed high errors that increased with prediction horizon.

IV. DISCUSSION AND CONCLUSION

Retrospective slice-level fetal MRI motion estimation and correction methods have evolved from hierarchical [12], [13] and slice intersection-based [14] methods to progressive [15], [16], [17], [20], patch-based [18], and more recently, dynamic motion tracking techniques [19]. Recent image-based MRI motion estimation techniques seek regularization through

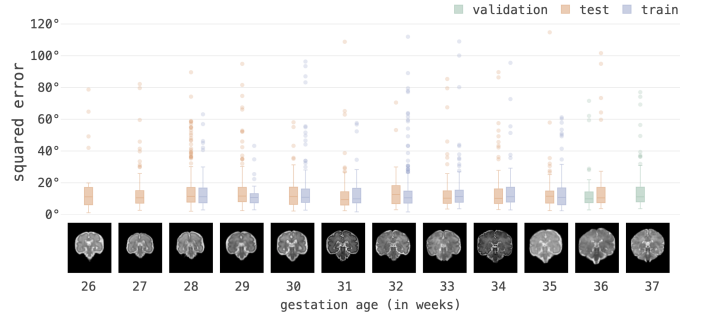


Figure 7: Average squared rotational error of one-step ahead prediction tasks for 10 timesteps grouped by GA. Consistent errors show that our model generalized well to variations in anatomy and GA outside of the domain and range that it was trained on.

modeling motion dynamics [7], or use parametric robust state space models to estimate relative position of sequentially-acquired slices [53], [54]. While the underlying phenomena are nonlinear, these techniques made simplifying assumptions to linearize the problem and used image registration along with state space estimation methods such as Kalman filtering (or its robust extensions) for motion tracking. Nonetheless, Bayesian filtering based Kalman filters fail to model nonlinear relationships as well as non-Gaussian noise, and their extended versions also fail when dynamics are highly nonlinear. These techniques are thus difficult to scale up to real life scenarios.

More capable Gaussian mixture models [55], process models [56] or dynamic Bayesian networks (DBN) [38] can accommodate complex dynamics but need strong priors by experts in their corresponding graph models, which makes them prone to the same practical issues that exist in conventional methods especially when long term prediction is desired. As a result of using image registration, these techniques are computationally intensive and cannot be easily applied in real-time. More importantly, none of the current techniques explic-

Timestep Masked	Baseline model error			Masked model error		
	Est	OSP	MSP	Est	OSP	MSP
No Mask	1.37	2.97	7.41	1.03	2.93	7.69
1	5.83	4.42	10.48	4.86	3.70	10.05
2	4.83	3.03	7.58	2.97	2.87	7.62
3	4.36	2.98	7.50	2.17	2.86	7.61
4	3.06	3.03	7.98	1.87	2.71	7.98
5	3.87	3.05	8.13	2.01	2.83	7.41
6	3.29	4.06	8.39	2.43	2.91	7.63
7	3.25	4.17	8.65	2.59	2.93	7.69
8	3.91	6.37	9.21	2.61	3.02	7.74
9	4.06	6.78	10.74	2.68	3.59	8.15
10	4.19	17.37	15.89	3.88	6.96	9.54

Table II: Results of a probing task on our full model trained with masked data against our model trained on unmasked data (baseline): mean squared rotational error of estimation (Est), one step (OSP) and multi-step prediction (MSP) on test set have been shown based on the timestep in which a slice was masked in the test sequence (first column). Results of both models on unmasked test data (first row) were similar, however the prediction performance of the baseline model indicates that to make predictions this model put a heavy weight on slices that appeared towards the end of the sequence. On the other hand, our full model trained with randomly-masked sequences, performed consistently regardless of the position of the masked slice in the sequence.

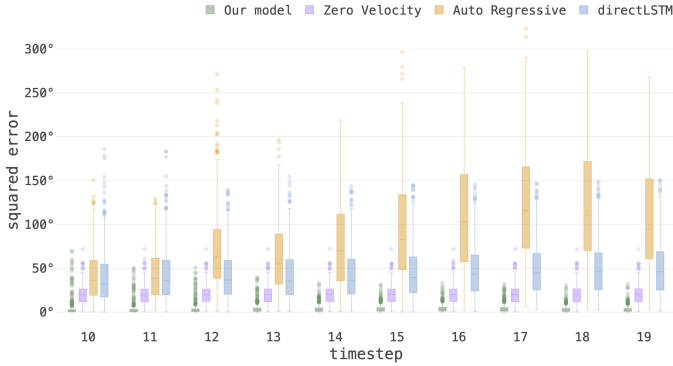


Figure 8: Squared error of multi-step prediction for the test data that involved volunteer motion patterns, shows the generalization efficacy of our model on real motion patterns. In all baseline models, the prediction error increased with the prediction steps due to compounding errors. It is seen that at the first timestep, the auto-regressive model generated a low error that was comparable to our model; but its error significantly increased for the subsequent timesteps. In comparison, due to the use of image context from spatial and temporal encoders, our model maintained low error in multi-step prediction.

itly uses image information and image recognition to model motion dynamics for 3D pose estimation. Registration-based methods are slow and offer a limited capture range, which makes them prone to failure when motion is continuous and large. In other words, even when integrated with state space estimation methods for dynamic motion tracking, registration-based techniques may not easily recover if they lose subject's position. This is especially problematic in motion estimation in fetal MRI as fetuses in the second and early third trimesters move frequently and rotate in large angles. Finally, almost all of the current methods rely on certain initialization assumptions such as the existence of a motion-free reference scan for registration, which is restrictive and unrealistic when considered for use in real-time applications.

In this paper we showed predictive potential of recurrent

neural networks for modeling end-to-end motion in MRI. To this end, we developed a combination of spatial encoders based on convolutional neural networks and temporal encoder and decoder networks based on CNN-LSTM to learn the spatiotemporal features of anatomy and slice sampling from imaging data to predict motion trajectories. Loss functions on multiple regression heads led to a robust model that generalized well beyond the training set to fetuses scanned at different ages and with motion of different patterns. Our technique is capable of estimating and predicting the 3D pose of the fetal brain in real-time despite large fetal movements. This technique, therefore, can shift focus from post acquisition slice registration and reordering to real-time navigated slice acquisition, which in-turn can lead to much more efficient, effective, and tolerable fetal MRI scan sessions. It can also play a critical role in real-time assessment of the quality of highly motion-sensitive scans such as fetal functional MRI to automatically adapt the length or duration of such scans.

REFERENCES

- [1] C. Malamateniou, S. Malik, S. Counsell, J. Allsop, A. McGuinness, T. Hayat, K. Broadhouse, R. Nunes, A. Ederies, J. Hajnal, and M. Rutherford, "Motion-compensation techniques in neonatal and fetal MR imaging," *American Journal of Neuroradiology*, vol. 34, no. 6, pp. 1124–1136, 2013.
- [2] O. Afacan, B. Erem, D. P. Roby, N. Roth, A. Roth, S. P. Prabhu, and S. K. Warfield, "Evaluation of motion and its effect on brain magnetic resonance image quality in children," *Pediatric radiology*, vol. 46, no. 12, pp. 1728–1735, 2016.
- [3] Boston Children's Hospital, "Partnering with families to minimize exposure to anesthesia," 2019, <https://thriving.childrenshospital.org/minimize-anesthesia-exposure/>, Last accessed on 2019-06-10.
- [4] J. G. Pipe, "Motion correction with PROPELLER MRI: application to head motion and free-breathing cardiac imaging," *Magnetic Resonance in Medicine: An Official Journal of the International Society for Magnetic Resonance in Medicine*, vol. 42, no. 5, pp. 963–969, 1999.
- [5] S. Thesen, O. Heid, E. Mueller, and L. R. Schad, "Prospective acquisition correction for head motion with image-based tracking for real-time fMRI," *Magnetic Resonance in Medicine: An Official Journal of the International Society for Magnetic Resonance in Medicine*, vol. 44, no. 3, pp. 457–465, 2000.
- [6] J. Maclaren, M. Herbst, O. Speck, and M. Zaitsev, "Prospective motion correction in brain imaging: a review," *Magnetic resonance in medicine*, vol. 69, no. 3, pp. 621–636, 2013.
- [7] N. White, C. Roddey, A. Shankaranarayanan, E. Han, D. Rettmann, J. Santos, J. Kuperman, and A. Dale, "PROMO: real-time prospective motion correction in MRI using image-based tracking," *Magnetic Resonance in Medicine: An Official Journal of the International Society for Magnetic Resonance in Medicine*, vol. 63, no. 1, pp. 91–105, 2010.
- [8] O. Afacan, T. E. Wallace, and S. K. Warfield, "Retrospective correction of head motion using measurements from an electromagnetic tracker," *Magnetic resonance in medicine*, 2019.
- [9] R. Frost, P. Wighton, F. I. Karahanoğlu, R. L. Robertson, P. E. Grant, B. Fischl, M. D. Tisdall, and A. van der Kouwe, "Markerless high-frequency prospective motion correction for neuroanatomical MRI," *Magnetic resonance in medicine*, vol. 82, no. 1, pp. 126–144, 2019.
- [10] T. E. Wallace, O. Afacan, M. Waszak, T. Kober, and S. K. Warfield, "Head motion measurement and correction using FID navigators," *Magnetic resonance in medicine*, vol. 81, no. 1, pp. 258–274, 2019.
- [11] A. Gholipour, J. A. Estroff, C. E. Barnewolt, R. L. Robertson, P. E. Grant, B. Gagoski, S. K. Warfield, O. Afacan, S. A. Connolly, J. J. Neil, A. Wolfberg, and R. V. Mulkern, "Fetal MRI: a technical update with educational aspirations," *Concepts in Magnetic Resonance Part A*, vol. 43, no. 6, pp. 237–266, 2014.
- [12] F. Rousseau, O. A. Glenn, B. Iordanova, C. Rodriguez-Carranza, D. B. Vigneron, J. A. Barkovich, and C. Studholme, "Registration-based approach for reconstruction of high-resolution in utero fetal MR brain images," *Academic radiology*, vol. 13, no. 9, pp. 1072–1081, 2006.

- [13] S. Jiang, H. Xue, A. Glover, M. Rutherford, D. Rueckert, and J. V. Hajnal, "MRI of moving subjects using multislice snapshot images with volume reconstruction (SVR): application to fetal, neonatal, and adult brain studies," *IEEE transactions on medical imaging*, vol. 26, no. 7, pp. 967–980, 2007.
- [14] K. Kim, P. A. Habas, F. Rousseau, O. A. Glenn, A. J. Barkovich, and C. Studholme, "Intersection based motion correction of multislice MRI for 3-D in utero fetal brain image formation," *IEEE transactions on medical imaging*, vol. 29, no. 1, pp. 146–158, 2010.
- [15] A. Gholipour, J. A. Estroff, and S. K. Warfield, "Robust super-resolution volume reconstruction from slice acquisitions: application to fetal brain MRI," *IEEE transactions on medical imaging*, vol. 29, no. 10, pp. 1739–1758, 2010.
- [16] M. Kuklisova-Murgasova, G. Quaghebeur, M. A. Rutherford, J. V. Hajnal, and J. A. Schnabel, "Reconstruction of fetal brain MRI with intensity matching and complete outlier removal," *Medical image analysis*, vol. 16, no. 8, pp. 1550–1564, 2012.
- [17] B. Kainz, M. Steinberger, W. Wein, M. Kuklisova-Murgasova, C. Malamatienou, K. Keraudren, T. Torsney-Weir, M. Rutherford, P. Aljabar, J. V. Hajnal *et al.*, "Fast volume reconstruction from motion corrupted stacks of 2D slices," *IEEE transactions on medical imaging*, vol. 34, no. 9, pp. 1901–1913, 2015.
- [18] A. Alansary, M. Rajchl, S. G. McDonagh, M. Murgasova, M. Damodaram, D. F. Lloyd, A. Davidson, M. Rutherford, J. V. Hajnal, D. Rueckert, and B. Kainz, "PVR: patch-to-volume reconstruction for large area motion correction of fetal MRI," *IEEE transactions on medical imaging*, vol. 36, no. 10, pp. 2031–2044, 2017.
- [19] B. Marami, S. S. M. Salehi, O. Afacan, B. Scherrer, C. K. Rollins, E. Yang, J. A. Estroff, S. K. Warfield, and A. Gholipour, "Temporal slice registration and robust diffusion-tensor reconstruction for improved fetal brain structural connectivity analysis," *NeuroImage*, vol. 156, pp. 475–488, 2017.
- [20] M. Ebner, G. Wang, W. Li, M. Aertsen, P. A. Patel, R. Aughwane, A. Melbourne, T. Doel, A. L. David, J. Deprest, S. Ourselin, and T. Vercauteren, "An automated localization, segmentation and reconstruction framework for fetal brain MRI," in *International Conference on Medical Image Computing and Computer-Assisted Intervention*. Springer, 2018, pp. 313–320.
- [21] E. Ferrante and N. Paragios, "Slice-to-volume medical image registration: A survey," *Medical image analysis*, vol. 39, pp. 101–123, 2017.
- [22] V. Taimouri, A. Gholipour, C. Velasco-Annis, J. A. Estroff, and S. K. Warfield, "A template-to-slice block matching approach for automatic localization of brain in fetal MRI," in *2015 IEEE 12th International Symposium on Biomedical Imaging (ISBI)*. IEEE, 2015, pp. 144–147.
- [23] A. Gholipour, C. K. Rollins, C. Velasco-Annis, A. Ouallam, A. Akhondi-Asl, O. Afacan, C. M. Ortinau, S. Clancy, C. Limperopoulos, E. Yang *et al.*, "A normative spatiotemporal mri atlas of the fetal brain for automatic segmentation and analysis of early brain growth," *Scientific reports*, vol. 7, no. 1, p. 476, 2017.
- [24] S. Tourbier, C. Velasco-Annis, V. Taimouri, P. Hagmann, R. Meuli, S. K. Warfield, M. B. Cuadra, and A. Gholipour, "Automated template-based brain localization and extraction for fetal brain MRI reconstruction," *NeuroImage*, vol. 155, pp. 460–472, 2017.
- [25] S. S. M. Salehi, S. Khan, D. Erdogmus, and A. Gholipour, "Real-time deep pose estimation with geodesic loss for image-to-template rigid registration," *IEEE transactions on medical imaging*, vol. 38, no. 2, pp. 470–481, 2018.
- [26] S. Hochreiter and J. Schmidhuber, "Long short-term memory," *Neural computation*, vol. 9, no. 8, pp. 1735–1780, 1997.
- [27] J. Wu, T. Xue, J. J. Lim, Y. Tian, J. B. Tenenbaum, A. Torralba, and W. T. Freeman, "Single image 3D interpreter network," in *European Conference on Computer Vision*. Springer, 2016, pp. 365–382.
- [28] G. Pavlakos, X. Zhou, A. Chan, K. G. Derpanis, and K. Daniilidis, "6-dof object pose from semantic keypoints," in *Robotics and Automation (ICRA), IEEE International Conference*. IEEE, 2017, pp. 2011–2018.
- [29] S. Tulsiani and J. Malik, "Viewpoints and keypoints," in *Proceedings of the IEEE Conference on Computer Vision and Pattern Recognition*, 2015, pp. 1510–1519.
- [30] H. Su, C. R. Qi, Y. Li, and L. J. Guibas, "Render for CNN: Viewpoint estimation in images using cnns trained with rendered 3d model views," in *Proceedings of the IEEE International Conference on Computer Vision*, 2015, pp. 2686–2694.
- [31] S. Mahendran, H. Ali, and R. Vidal, "3D pose regression using convolutional neural networks," in *IEEE International Conference on Computer Vision*, vol. 1, no. 2, 2017, p. 4.
- [32] A. Newell, K. Yang, and J. Deng, "Stacked hourglass networks for human pose estimation," in *European Conference on Computer Vision*. Springer, 2016, pp. 483–499.
- [33] R. Alp Güler, N. Neverova, and I. Kokkinos, "Densepose: Dense human pose estimation in the wild," in *Proceedings of the IEEE Conference on Computer Vision and Pattern Recognition*, 2018, pp. 7297–7306.
- [34] M. Andriluka, U. Iqbal, E. Insafutdinov, L. Pishchulin, A. Milan, J. Gall, and B. Schiele, "Posetrack: A benchmark for human pose estimation and tracking," in *Proceedings of the IEEE Conference on Computer Vision and Pattern Recognition*, 2018, pp. 5167–5176.
- [35] B. Hou, A. Alansary, S. McDonagh, A. Davidson, M. Rutherford, J. V. Hajnal, D. Rueckert, B. Glocker, and B. Kainz, "Predicting slice-to-volume transformation in presence of arbitrary subject motion," in *International Conference on Medical Image Computing and Computer-Assisted Intervention*. Springer, 2017, pp. 296–304.
- [36] B. Hou, B. Khanal, A. Alansary, S. McDonagh, A. Davidson, M. Rutherford, J. V. Hajnal, D. Rueckert, B. Glocker, and B. Kainz, "3-D reconstruction in canonical co-ordinate space from arbitrarily oriented 2-D images," *IEEE transactions on medical imaging*, vol. 37, no. 8, pp. 1737–1750, 2018.
- [37] D. E. Rumelhart, G. E. Hinton, and R. J. Williams, "Learning representations by back-propagating errors," *Cognitive modeling*, vol. 5, no. 3, 1988.
- [38] T. Gindele, S. Brechtel, and R. Dillmann, "Learning driver behavior models from traffic observations for decision making and planning," *IEEE Intelligent Transportation Systems Magazine*, vol. 7, pp. 69–79, 2015.
- [39] I. Sutskever, O. Vinyals, and Q. V. Le, "Sequence to sequence learning with neural networks," in *Advances in neural information processing systems*, 2014, pp. 3104–3112.
- [40] P. Ondruska and I. Posner, "Deep tracking: Seeing beyond seeing using recurrent neural networks," in *AAAI Conference on Artificial Intelligence*, 2016.
- [41] S. Krebs, B. Duraisamy, and F. Flohr, "A survey on leveraging deep neural networks for object tracking," *2017 IEEE 20th International Conference on Intelligent Transportation Systems*, pp. 411–418, 2017.
- [42] D. Held, S. Thrun, and S. Savarese, "Learning to track at 100 fps with deep regression networks," in *European Conference on Computer Vision*. Springer, 2016, pp. 749–765.
- [43] J. Valmadre, L. Bertinetto, J. Henriques, A. Vedaldi, and P. H. Torr, "End-to-end representation learning for correlation filter based tracking," in *Proceedings of the IEEE Conference on Computer Vision and Pattern Recognition*, 2017, pp. 2805–2813.
- [44] B. Li, J. Yan, W. Wu, Z. Zhu, and X. Hu, "High performance visual tracking with siamese region proposal network," in *Proceedings of the IEEE Conference on Computer Vision and Pattern Recognition*, 2018, pp. 8971–8980.
- [45] G. Ning, Z. Zhang, C. Huang, X. Ren, H. Wang, C. Cai, and Z. He, "Spatially supervised recurrent convolutional neural networks for visual object tracking," in *2017 IEEE International Symposium on Circuits and Systems (ISCAS)*. IEEE, 2017, pp. 1–4.
- [46] D. Gordon, A. Farhadi, and D. Fox, "Re3: Real-time recurrent regression networks for visual tracking of generic objects," *IEEE Robotics and Automation Letters*, vol. 3, no. 2, pp. 788–795, 2018.
- [47] C. Xu, C. Lu, X. Liang, J. Gao, W. Zheng, T. Wang, and S. Yan, "Multi-loss regularized deep neural network," *IEEE Transactions on Circuits and Systems for Video Technology*, vol. 26, no. 12, pp. 2273–2283, 2016.
- [48] S. S. M. Salehi, S. R. Hashemi, C. Velasco-Annis, A. Ouallam, J. A. Estroff, D. Erdogmus, S. K. Warfield, and A. Gholipour, "Real-time automatic fetal brain extraction in fetal mri by deep learning," in *2018 IEEE 15th International Symposium on Biomedical Imaging (ISBI 2018)*. IEEE, 2018, pp. 720–724.
- [49] S. S. M. Salehi, D. Erdogmus, and A. Gholipour, "Auto-context convolutional neural network (auto-net) for brain extraction in magnetic resonance imaging," *IEEE transactions on medical imaging*, vol. 36, no. 11, pp. 2319–2330, 2017.
- [50] P. A. Yushkevich, J. Piven, H. C. Hazlett, R. G. Smith, S. Ho, J. C. Gee, and G. Gerig, "User-guided 3D active contour segmentation of anatomical structures: significantly improved efficiency and reliability," *Neuroimage*, vol. 31, no. 3, pp. 1116–1128, 2006.
- [51] A. Gholipour, M. Polak, A. Van Der Kouwe, E. Nevo, and S. K. Warfield, "Motion-robust MRI through real-time motion tracking and retrospective super-resolution volume reconstruction," in *2011 Annual International Conference of the IEEE Engineering in Medicine and Biology Society*. IEEE, 2011, pp. 5722–5725.

- [52] J. Martinez, M. J. Black, and J. Romero, "On human motion prediction using recurrent neural networks," in *Proceedings of the IEEE Conference on Computer Vision and Pattern Recognition*, 2017, pp. 2891–2900.
- [53] B. Marami, B. Scherrer, O. Afacan, B. Erem, S. K. Warfield, and A. Gholipour, "Motion-robust diffusion-weighted brain MRI reconstruction through slice-level registration-based motion tracking," *IEEE Trans. Med. Imaging*, vol. 35, no. 10, pp. 2258–2269, 2016.
- [54] B. Marami, B. Scherrer, S. Khan, O. Afacan, S. Prabhu, M. Sahin, S. Warfield, and A. Gholipour, "Motion-robust diffusion compartment imaging using simultaneous multi-slice acquisition," *Magnetic resonance in medicine*, vol. 81, no. 5, p. 3314, 2019.
- [55] S. Ammoun and F. Nashashibi, "Real time trajectory prediction for collision risk estimation between vehicles," *2009 IEEE 5th International Conference on Intelligent Computer Communication and Processing*, pp. 417–422, 2009.
- [56] J. Wiest, M. Höffken, U. Kressel, and K. C. J. Dietmayer, "Probabilistic trajectory prediction with gaussian mixture models," *2012 IEEE Intelligent Vehicles Symposium*, pp. 141–146, 2012.